Inorg. Chem. **2008**, *47*, 8044−8052

Synthesis and Structures of a New Series of Silver-Vanadate Hybrid Solids and Their Optical and Photocatalytic Properties

Haisheng Lin and Paul A. Maggard*

Department of Chemistry, North Carolina State University, Raleigh, North Carolina 27695-8204

Received March 7, 2008

Three new silver-vanadate hybrid solids, $[Ag(bpy)]_4V_4O_{12}\cdot 2H_2O$ (**I**), $[Ag(dpa)]_4V_4O_{12}\cdot 4H_2O$ (**II**), and $Ag_4(pzc)_2V_2O_6$ (**III**) (bpy = 4,4′-bipyridine, dpa = 1,2-bis(4-pyridyl)-ethane, pzc = pyrazinecarboxylate), were synthesized by hydrothermal methods and characterized using single crystal X-ray diffraction (**I**, $P2_1/c$, $Z = 4$, $a = 11.375(2)$ Å, $b = 14.281(4)$ Å, $c = 13.598(3)$ Å, $\beta = 91.46(1)°$; **II**, $P2_1/c$, $Z = 8$, $a = 13.5748(3)$ Å, $b = 15.3372(4)$ Å, $c = 14.1854(3)$ Å, $\beta = 114.1410(9)°$; **III**, $P\bar{1}$, $Z = 2$, $a = 3.580(1)$ Å, $b = 11.839(4)$ Å, $c = 19.321(7)$ Å, $\alpha = 89.110(7)°$, $\beta = 87.719(9)°$, $\gamma = 86.243(8)°$), thermogravimetric analysis, and UV−vis diffuse reflectance. The structures of **I** and **II** are constructed from neutral $\{Ag_4V_4O_{12}\}_n$ layers of clusters that are pillared via the coordination of organic ligands (bpy for **I** and dpa for **II**) to the Ag sites in each layer. Conversely, the structure of **III** is composed of a three-dimensional $\{Ag_2(pzc)^+\}_n$ coordination network with channels containing $\{VO_3^-\}_n$ chains. The lattice water molecules can be removed upon heating to ≥180 °C for **I** (reversibly) and to ≥120 °C for **II** (irreversibly). All three decompose with the removal of organic ligands at higher temperatures of >200−300 °C. Their optical bandgap sizes were measured to be 2.77 eV for **I**, 2.95 eV for **II**, and 2.45 eV for **III**, which decrease most notably as a result of the band widening for the more extended vanadate structure in **III**. All three hybrid solids are photocatalytically active for the decomposition of methylene blue under UV light (λ < 400 nm; 1.01, 0.64, and 2.65 mg L^{-1} h^{-1} for **I**, **II**, and **III**, respectively), while only **III** exhibits a high activity under visible-light irradiation (λ > 400 nm; 1.20 mg L^{-1} h^{-1}). These new hybrid solids are among the first reported to exhibit high photocatalytic activities under either ultraviolet or visible-light irradiation and have also been analyzed with respect to the effect of the different organic ligands on their atomic- and electronic-structures.

Introduction

Hybrid solids that combine both metal-oxide and organic ligand "building blocks" are a growing class of new materials that are beginning to receive widespread attention because of their potential to express, within the same compound, both the robustness and physical properties of metal oxides in conjunction with the versatility and chemical flexibility of organic ligands.[1] This chemical synergy can yield new routes to a plethora of novel structures and properties with many potential applications, such as in those explored for absorbent, catalytic, and sensor-related properties.[2] In addition, "retrosynthetic" analyses of their structures have enabled new progress toward rational synthetic principles to aid in targeting specific structural features.[3] Specific recent examples from our group include the layered rhenates $M_2(pzc)_2(H_2O)_xReO_4$ (M = Co, Ni, Cu; pzc = pyrazinecarboxylate),[4−6] $MReO_4(pyz)$ (M = Ag, Cu; pyz = pyrazine),[7,8] layered molybdate hybrids such as $[M_2(pzc)_2(H_2O)_x][Mo_5O_{16}]$

* To whom correspondence should be addressed. E-mail: paul_maggard@ncsu.edu. Phone: (+1) 919-515-3616. Fax: (+1) 919-515-5079.

(1) (a) Zheng, L.-M.; Whitfield, T.; Wang, X.; Jacobson, A. J. *Angew.Chem., Int.Ed.* **2000**, *39* (24), 4528–4531. (b) Kong, Z.; Weng, L.; Tan, D.; He, H.; Zhang, B.; Kong, J.; Yue, B. *Inorg. Chem.* **2004**, *43* (18), 5676–5680. (c) Maggard, P. A.; Boyle, P. D. *Inorg. Chem.* **2003**, *42*, 4250–4252. (d) Hagrman, P. J.; Hagrman, D.; Zubieta, J. *Angew.Chem., Int.Ed.* **1999**, *38* (18), 2639–2684.

(2) (a) Cheetham, A. K. *Science* **1994**, *264* (5160), 794–795. (b) Pope, M. T.; Müller, A. *Angew. Chem., Int. Ed. Engl.* **1991**, *30* (1), 34–48. (c) Xu, L.; Qin, C.; Wang, X.; Wei, Y.; Wang, E. *Inorg. Chem.* **2003**, *42* (23), 7342–7344. (d) Müller, A.; Reuter, H.; Dillinger, S. *Angew. Chem., Int. Ed. Engl.* **1995**, *34* (21), 2328–2361. (e) Yaghi, O. M.; Li, H.; Davis, C.; Richardson, D.; Groy, T. L. *Acc. Chem. Res.* **1998**, *31* (18), 474–484. (f) Li, H.; Eddaoudi, M.; Groy, T. L.; Yaghi, O. M. *J. Am. Chem. Soc.* **1998**, *120* (33), 8571–8572.

(3) Yan, B.; Maggard P. A. *Inorganic Chemistry in Focus*, III ed.; Meyer, G., Naumann, D., Weseman, L., Eds.; Wiley-VCH: Weinheim, 2006; Vol. *17*, pp 251−266.

(4) Maggard, P. A.; Yan, B.; Luo, J. *Angew. Chem., Int. Ed. Engl.* **2005**, *44*, 2553–2556.

10.1021/ic8004129 CCC: $40.75
Published on Web 08/13/2008

(M = Co, Ni),[9] and the vanadate hybrids $M(pyz)V_4O_{10}$ (M = Co, Ni, Zn)[10,11] and $M(bpy)V_4O_{10}$ (M = Ag, Cu).[12] The structural flexibility of the latter hybrid solids, for example, has helped to probe the underlying theories of strongly correlated electrons and the magnetic properties of vanadate layers.

Our current research efforts continue to focus on the synthesis of new heterometallic-oxides/organics containing both early (V^{5+}, Mo^{6+}, Re^{7+}) and late (Cu^+, Ag^+) transition metals in combination with structure-directing organic ligands that will coordinate preferentially to the late transition-metal sites. This selection of early/late transition metals is useful for probing the structural and electronic origins of the bandgap sizes of heterometallic oxides that arise from a Metal-to-Metal Charger Transfer (MMCT) between the d^{10} (e.g., Ag^+) and d^0 (e.g., V^{5+}) electron configurations. Previous investigations, such as reported for $AgMO_3$ (M = Nb, Ta) and $AgVO_3$,[13,14] have revealed that these MMCT transitions between d^{10}/d^0 electron configurations are the cause of their photocatalytic activities in the light-driven production of H_2 and/or O_2 in aqueous solutions. Further, these transitions can lead to the absorption of lower-energy visible light in metal-oxides owing to an ~1.5−0.5 eV decrease in their band gap sizes, relative to the alkali metal versions, which arises from the Ag/Cu ($3d^{10}/4d^{10}$ orbitals) mixing into and raising the valence band energies. However, current photocatalytic investigations into solids with this type of electronic structure have been limited to only condensed metal-oxides prepared by conventional solid-state methods.

Research into hybrid solids has served to significantly expand the structural diversity of heterometallic-oxides/organics that contain a combination of d^0 with d^{10} transition metals, wherein a greater structural flexibility and control can be used to probe the origins of their optical and photocatalytic properties. For example, our group has demonstrated that "$AgReO_4$" layers of the parent $AgReO_4$ solid can be pillared by bridging organic or metal-coordinated ligands, leading to hybrid solids that exhibit microporosity or chirality in $M(pzc)_2(H_2O)_2AgReO_4$ and $Cu(pzc)_2AgReO_4$, respectively.[4,6] In these examples, the water molecules that are coordinated to the axial sites of the $M(pzc)_2$ pillars can be reversibly removed to generate coordinatively-unsaturated metal sites without the loss of crystallinity. At higher temperatures (>300 °C) the organic ligands are typically liberated to yield either the parent phases or amorphous reduced materials. In another example, we have recently reported on the syntheses and optical properties of copper(I)−rhenate hybrids, $CuReO_4(pyz)$ and $Cu_3ReO_4(q6c)_2$.[8] These hybrid solids have much smaller optical bandgap sizes of ~2.2 eV and also yield the new $CuReO_4$ parent phase upon removal of the ligands. However, these new rhenate hybrids have not been found to exhibit high photocatalytic activities under the testing conditions investigated to date.

Described herein is the synthesis and characterization of the first known series of photocatalytically active silver-vanadate hybrids, $[Ag(bpy)]_4V_4O_{12}\cdot 2H_2O$ (**I**), $[Ag(dpa)]_4V_4O_{12}\cdot 4H_2O$ (**II**), and $Ag_4(pzc)_2V_2O_6$ (**III**). All three compounds are composed of silver-vanadate layered or network structures that are pillared at the silver sites by the coordinating organic ligands. Further, their atomic structures and optical properties are analyzed with respect to their calculated electronic structures. These analyses are used to understand the trends leading to smaller optical bandgap sizes, as well as their resulting photocatalytic activities for the decomposition of methylene blue (MB) under both ultraviolet and visible light.

Experimental Section

Synthetic Approach. Each hybrid solid was synthesized under hydrothermal conditions by heat-sealing all reactants into an FEP Teflon pouch (3″ × 4″). Starting materials included Ag_2O (99+% metal basis, Alfa Aesar), NH_4VO_3 (purified grade, Fisher), 4,4′-bipyridine (98%, Alfa Aesar), 1,2-bis(4-pyridyl)-ethane (99%, Aldrich) and pyrazine-2-carboxylic acid (98%, Alfa Aesar). A reagent amount of 3.0 M NH_3(aq) solution was also added to the solvent in each of the reactions. The heat-sealed pouches were then placed inside a 125 mL Teflon-lined stainless-steel reaction vessel which was backfilled with ~40 mL of deionized water before closing. After heating the reaction vessel to 105−150 °C for 1−3 days, it was slowly cooled to room temperature at 6 °C·h^{-1}. The products were then filtered, washed with deionized water, and dried in air. The phase purities and crystallinities of the compounds were checked by powder X-ray diffraction using an Inel XRG 3000 diffractometer (Cu Kα radiation, $\lambda = 1.5406$ Å), and these results are given in the Supporting Information.

Synthesis of $[Ag(bpy)]_4V_4O_{12}\cdot 2H_2O$ (I). A stoichiometric mixture of 4,4′-bipyridine (31.3 mg, 0.20 mmol), Ag_2O (23.2 mg, 0.10 mmol), NH_4VO_3 (23.4 mg, 0.20 mmol), and 3 M NH_3(aq) (0.2 g, 10.2 mmol) was heat sealed into an FEP Teflon pouch. The reactants were heated at 150 °C for 1−3 days inside a convection oven. The products were pale yellow bar-shaped crystals. Yield: ~85% based on Ag.

Synthesis of $[Ag(dpa)]_4V_4O_{12}\cdot 4H_2O$ (II). A stoichiometric amount of dpa (36.8 mg, 0.20 mmol), Ag_2O (23.2 mg, 0.10 mmol), NH_4VO_3 (23.4 mg, 0.20 mmol), and 3 M NH_3(aq) (0.4 g, 20.4 mmol) was loaded and heated inside the hydrothermal reaction vessel at 105 °C for 24 h within a convection oven. Pale yellow needle-like crystals were obtained. Yield: ~79% based on Ag.

Synthesis of $Ag_4(pzc)_2V_2O_6$ (III). This hybrid solid was similarly prepared by heating a stoichiometric mixture of Hpzc (24.8 mg, 0.20 mmol), Ag_2O (46.4 mg, 0.20 mmol), NH_4VO_3 (23.4 mg, 0.20 mmol), and 3 M NH_3(aq) (0.4 g, 20.4 mmol) at 150 °C for 3 days inside a convection oven. Gold-yellow needle crystals were obtained. Yield: ~91% based on Ag.

Crystallographic Structure Determination. A bar-shaped crystal (0.32 × 0.10 × 0.02 mm) of **I** was mounted onto a glass fiber with a small amount of epoxy. All X-ray measurements were

(5) Luo, J.; Alexander, B.; Wagner, T. R.; Maggard, P. A. *Inorg. Chem.* **2004**, *43*, 5337–5542.
(6) Yan, B.; Capracotta, M. D.; Maggard, P. A. *Inorg. Chem.* **2005**, *44*, 6509–6511.
(7) Lin, H.; Yan, B.; Boyle, P. D.; Maggard, P. A. *J. Solid State Chem.* **2006**, *179*, 39–47.
(8) Lin, H.; Maggard, P. A. *Inorg. Chem.* **2007**, *46*, 1283–1290.
(9) Yan, B.; Maggard, P. A. *Inorg. Chem.* **2006**, *45*, 4721–4727.
(10) Yan, B.; Maggard, P. A. *J. Am. Chem. Soc.* **2007**, *129*, 12646–12647.
(11) Yan, B.; Luo, J.; Greedan, J. E.; Maggard, P. A. *Inorg. Chem.* **2006**, *45*, 5109–5118.
(12) Yan, B.; Maggard, P. A. *Inorg. Chem.* **2007**, *46*, 6640–6646.
(13) Kato, H.; Kobayashi, H.; Kudo, A. *J. Phys. Chem. B* **2002**, *106*, 12441–12447.
(14) Konta, R.; Kato, H.; Kobayashi, H.; Kudo, A. *Phys. Chem. Chem. Phys.* **2003**, *5*, 3061–3065.

Table 1. Selected Single Crystal and Structure Refinement Details for $[Ag(bpy)]_4V_4O_{12}\cdot 2H_2O$ (**I**), $[Ag(dpa)]_4V_4O_{12}\cdot 4H_2O$ (**II**) and $Ag_4(pzc)_2V_2O_6$ (**III**)

	I	II	III
formula	$C_{20}H_{18}Ag_2N_4O_7V_2$	$C_{12}H_{14}AgN_2O_4V$	$C_{10}H_6Ag_4N_4O_{10}V_2$
formula weight (g/mol)	744.00	409.06	875.55
crystal color, habit	pale-yellow, bar	pale-yellow, prism	yellow, needle
crystal system	monoclinic	monoclinic	triclinic
space group, Z	$P2_1/c$, 4	$P2_1/c$, 8	$P\bar{1}$, 2
temperature, K	293	110	193
a, Å	11.375(2)	13.5748(3)	3.580(1)
b, Å	14.281(4)	15.3372(4)	11.839(4)
c, Å	13.598(3)	14.1854(3)	19.321(7)
α, deg	90.0	90.0	89.110(7)
β, deg	91.462(10)	114.1410(9)	87.719(9)
γ, deg	90.0	90.0	86.243(8)
V, Å^3	2208.1(9)	2695.1(1)	816.4(5)
ρ, (g/cm)	2.238	2.016	3.561
λ(Mo Kα), Å	0.71073	0.71073	0.71073
μ, (mm^{-1})	2.62	2.16	5.870
total reflections, R(int)	117284, 0.040	62597, 0.027	5725,0.0299
data/restraints/parameters	4828/0/307	10269/0/361	4525/228/274
R1, wR2[a][$I > 2\ \sigma(I)$]	0.038, 0.043	0.031,0.043	0.0678, 0.1758

[a] $R_f = \sum||F_o| - |F_c||/\sum|F_o|$; $R_w = [\sum(w(F_o^2 - F_c^2)^2)/(\sum(F_o^2)^2)\ ]^{1/2}$; $w = \sigma_F^{-2}$.

made on a Bruker-Nonius X8 Apex2 CCD diffractometer at 293 K. The unit cell dimensions were determined from a symmetry constrained fit of 8090 reflections with $5.70° < 2\theta < 53.93°$. The data collection strategy included both ω and φ scans that collected data up to 54.1° (2θ). The integration of frames was performed using the SAINT program.[15] The resulting raw data were scaled and corrected for absorption using a multiscan averaging of symmetry-equivalent data using the SADABS program.[16] The structure was solved by direct methods using SIR92.[17] The biphenyl hydrogen atoms were introduced at idealized positions and were allowed to ride on the parent carbon atoms. The final anisotropic structure refinement reached convergence, and the final structure refinement and atomic coordinate tables were created using the NRCVAX crystallographic program suite.[18]

A single crystal of **II** was selected and mounted on a nylon loop with a small amount of NVH immersion oil. All X-ray measurements were made on a Bruker-Nonius X8 Apex2 diffractometer at a temperature of 110 K. The unit cell dimensions were determined from a symmetry constrained fit of 9896 reflections with $5.32° < 2\theta < 66.12°$. The data collection strategy included both ω and φ scans that collected data up to 66.32° (2θ). The frame integration was performed using the SAINT program.[15] The resulting raw data were scaled and absorption corrected using a multiscan averaging of symmetry-equivalent data using SADABS.[16] The structure was solved by direct methods using the SIR97 program.[17] The hydrogen atoms were introduced at idealized positions and were allowed to ride on the parent atom. The final anisotropic structure refinement reached convergence, and the final structure refinement and atomic coordinate tables were taken from the NRCVAX crystallographic program suite.[18]

A single crystal of **III** was mounted on a nylon loop for data collection on a Bruker SMART APEX CCD diffractometer at a temperature of 193 K. The unit cell parameters were determined using 4525 reflections in the range of $8.04 < 2\theta < 55.0$. The structure was solved and refined using SHELXTL-97 in the triclinic space group $P\bar{1}$.[19] The hydrogen atoms on the pzc rings were refined in idealized positions at a C−H distance of 0.95Å.

Selected data collection and refinement parameters for all three crystals are listed in Table 1. The atomic coordinates and isotropic-equivalent displacement parameters of **I**, **II**, and **III** are given in the Supporting Information in Tables S1, S2, and S3, respectively. Interatomic contacts for selected bonds and angles for all three structures are listed in Table 2. Included in the Supporting Information is a complete list of data collection, refinement, and anisotropic displacement parameters and all near-neighbor interatomic distances and angles.

Thermogravimetric Analyses. Weighed samples (23.4 mg of **I**, 17.4 mg of **II**, and 12.4 mg of **III**) of each compound were loaded onto Pt pans, equilibrated, and tarred at room temperature and heated at a rate of 1 to 5 °C/min to 600 °C under flowing nitrogen on a TA Instruments TGA Q50.

Optical Bandgap Measurements. The UV−vis diffuse reflectance spectra were measured on a Cary 300 spectrophotometer equipped with an integrating sphere. Approximately 50 mg of powder of each sample was mounted onto a fused-silica holder and placed along the external window of the integrating sphere. A pressed polytetrafluoroethylene powder was used as a reference, and the data were plotted as the remission function $F(R_\infty) = (1 - R_\infty)^2/(2R_\infty)$, where R is the diffuse reflectance based on the Kubelka−Monk theory of diffuse reflectance.

Electronic Band Structure Calculations. Extended Hückel electronic structure calculations were carried out within the tight binding approximation using the CAESAR2 program,[20] using the full structures at 960 k-points spread over the irreducible wedge. The internal double-ζ basis sets were selected for the atomic orbital parameters, and the atomic coordinates and lattice dimensions were imported from their respective crystal structures.

Photocatalytic Reactions. Methylene Blue (MB) is often used as model dye contaminant to evaluate the activity of photocatalysts

(15) Bruker-Nonius, *SAINT+*, version 7.07B; Bruker-Nonius: Madison, WI, 2004.
(16) Bruker-Nonius, *SADABS*, version 2.10; Bruker-Nonius: Madison, WI, 2004.
(17) Altomare, A.; Burla, M. C.; Camalli, G.; Cascarano, G.; Giacovazzo, C.; Guagliardi, A.; Polidori, G. *J. Appl. Crystallogr.* **1994**, *27*, 435–436.
(18) Gabe, E. J.; Le Page, Y.; Charland, J.-P.; Lee, F. L.; White, P. S. *J. Appl. Crystallogr.* **1989**, *22*, 384–387.
(19) Sheldrick, G. M. *SHELXTL NT ver. 5.10, Software Package for Refinement of Crystal Structures*; Bruker Analytical X-ray Instruments, Inc.: Madison,WI, 1998.
(20) Whangbo, M.-H. *CAESAR*; Department of Chemistry, North Carolina State University: Raleigh, NC, 1998.
(21) Hormillosa, C. *Bond Valence Calculator*, version 2.0; McMaster University: Hamilton, Ontario, Canada, 1993.

Table 2. . Selected Interatomic Distances (Å) and Bond Valence Sums for **I**, **II**, and **III**[a]

atom1	atom2	distance, Å	atom1	atom2	distance, Å
		$[Ag(bpy)]_4V_4O_{12}\cdot 2H_2O$ (**I**)			
V1	O1	1.647(3)	Ag1	N1	2.178(3)
	O2	1.636(3)		N2	2.181(3)
	O3	1.800(3)		O2	2.739(3)
	O6	1.809(3)		O5	2.674(3)
	$\sum S_{ij}$	5.09	Ag2	N1′	2.181(3)
V2	O3	1.800(3)		N2′	2.161(3)
	O4	1.628(3)		O2	2.854(3)
	O5	1.639(3)		O4	2.751(3)
	O6	1.796(3)		O5	2.859(3)
	$\sum S_{ij}$	5.19		Ag1	3.189(1)
		$[Ag(dpa)]_4V_4O_{12}\cdot 4H_2O$ (**II**)			
V1	O1	1.797(1)	Ag1	N3	2.172(2)
	O2	1.640(1)		N4	2.173(2)
	O3	1.643(2)		O3	2.699(2)
	O4	1.821(1)		O6	2.689(2)
	$\sum S_{ij}$	5.06	Ag2	N1	2.178(2)
V2	O1	1.801(1)		N2	2.176(2)
	O4	1.828(1)		O3	2.633(2)
	O5	1.639(2)		O5	2.641(2)
	O6	1.641(1)		O6	2.625(2)
	$\sum S_{ij}$	5.05		Ag1	3.173(1)
		$Ag_4(pzc)_2V_2O_6$ (**III**)			
V1	O5	1.695(10)	Ag2	N2	2.311(13)
	O6	1.625(11)		O4	2.409(9)
	O7	1.890(9)		O4	2.693(9)
	O7	1.901(10)		O5	2.385(9)
	O7	2.031(10)		O5	2.648(9)
	$\sum S_{ij}$	5.05	Ag3	N4	2.343(12)
				O3	2.326(10)
V2	O8	1.692(9)		O3	2.481(10)
	O9	1.887(11)		O5	2.434(9)
	O9	1.906(10)		O5	2.653(9)
	O9	2.019(10)	Ag4	N3	2.278(11)
	O10	1.610(11)		O2	2.354(11)
	$\sum S_{ij}$	5.15		O8	2.348(9)
Ag1	N1	2.354(14)		O8	2.476(12)
	O1	2.361(10)	Ag1	Ag4	2.973(2)
	O1	2.546(9)	Ag2	Ag3	2.924(2)
	O1	2.606(9)			
	O8	2.416(9)			

[a] $S_{ij} = \exp[(R_0 - R_{ij})/B]$, $B = 0.37$, and $R_0 = 1.803$ Å for V^V.[21]

in the purification of dye wastewater.[22] It is reportedly very difficult to degrade this organic dye under visible light.[23−25] Herein, MB was used as a model organic pollutant to evaluate the activities of the hybrid photocatalytic solids. The photocatalytic activity of each sample for the decomposition of MB was measured by suspending a weighed amount (150 mg) of the powdered samples in an aqueous solution of MB (6.0 mg/L, 50 mL) in an ∼60 mL cylindrical vessel. This mixture was stirred continuously under ultraviolet ($\lambda < 400$ nm) or visible-light ($\lambda < 400$ nm) irradiation from a 400 W high-pressure Xe arc lamp (focused through a shutter window), which was equipped with a heat filter to remove infrared radiation and with cutoff filters to select for the desired wavelength ranges. The reactions were stopped at 15 min intervals to determine the concentrations of the aqueous MB solutions by UV−vis spectroscopy (HP 8453) at $\lambda = 655$ nm.

Results and Discussion

Structural Descriptions. The structures of $[Ag(bpy)]_4V_4O_{12}\cdot 2H_2O$ (**I**) and $[Ag(dpa)]_4V_4O_{12}\cdot 4H_2O$ (**II**) (bpy = 4,4′-bipyridine, dpa = 1,2-bis(4-pyridyl)-ethane) share many general structural similarities, as shown in Figure 1. In addition, both share the same space group ($P2_1/c$). Both **I** and **II** are composed of neutral $\{Ag_4V_4O_{12}\}_n$ layers of clusters that are pillared via coordination by the organic ligands (bpy for **I**, dpa for **II**) to the Ag sites between layers, shown as the blue polyhedra in Figure 1. The heterometallic $\{Ag_4V_4O_{12}\}_n$ layers consist of isolated $\{V_4O_{12}\}^{4-}$ tetramer rings that are linked together by eight nearest Ag^+ cations per ring to yield the layer structures shown in Figure 2 (A and B). Each $\{V_4O_{12}\}^{4-}$ ring is constructed from four corner-shared VO_4 tetrahedra with V−O bond distances within the expected ranges of 1.63−1.83Å, listed in Table 2.

In both **I** and **II** there are two symmetry-unique Ag sites, Ag1 and Ag2 in Figure 2 (A and B). In each layer, Ag1 is coordinated to two terminal oxygen atoms from separate $\{V_4O_{12}\}^{4-}$ rings at Ag−O distances of 2.739(3)Å and 2.674(4) Å for **I** and 2.699(2) Å and 2.689(2) Å for **II**. The Ag1 atoms are also bonded to two nitrogen groups from the organic ligands (bpy for **I**, dpa for **II**) from above and below each layer at ∼2.17 Å, to complete a $\{AgO_2N_2\}$ distorted square-planar coordination geometry. The Ag2 atoms in each structure coordinate to three terminal oxygen atoms from two separate $\{V_4O_{12}\}^{4-}$ clusters, with a range of Ag−O distances of 2.751(3)−2.859(3)Å for **I** and 2.625(2)−2.641(2)Å for **II**. The Ag2 atoms are also bonded to two nitrogen groups from the respective organic ligands, both above and below each layer, to give a $\{AgO_3N_2\}$ distorted trigonal-bipyramidal coordination geometry. For each structure, the coordination of the bridging organic ligands to the Ag sites results in extended 1D chains, that is, $\{Ag(L)^+\}_n$, along the [100] direction of the unit cells. The Ag1 and Ag2 atoms occur as relatively close pairs of dimers with Ag−Ag distances of 3.189(1) Å in **I** and 3.173(1) Å in **II**, shown in Figure 3. These pairs are a result of the face-to-face arrangement of the $\{Ag1(L)^+\}_n$ and $\{Ag2(L)^+\}_n$ chains, as expected for π-π stacking interactions of ligands that can help to stabilize the full three-dimensional network. One primary structural difference between **I** and **II** is found in the packing arrangement of the Ag−Ag dimer subunits. In the layers of **I**, infinite Ag1−O−Ag2 chains occur that are bridged via $\{V_4O_{12}\}^{4-}$ rings. In **II** the Ag1/Ag2 polyhedra are also similarly edge-shared, but here their packing only yields isolated dimers that are more fully separated by the tetrameric $\{V_4O_{12}\}^{4-}$ rings.

Another key aspect of **I** and **II** is that, although they share similar layered structures, they contain differing amounts of internal water molecules that can interact via hydrogen bonding. This difference is caused by the relatively shorter bpy bridging ligand for **I** that leads to a shorter *a*-axis length

(22) (a) Tsumura, T.; Kojitan, N.; Izumi, I.; Iwashita, N.; Toyoda, M.; Inagaki, M. *J. Mater. Chem.* **2002**, *12*, 1391. (b) Herrmann, J. M.; Disdier, J.; Pichat, P. *J. Catal.* **1988**, *113*, 72. (c) Li, X. Z.; Li, F. B. *Environ. Sci. Technol.* **2001**, *35*, 2381. (d) Muggli, D. S.; Ding, L.; Odland, M. J. *Catal. Lett.* **2002**, *78*, 23. (e) Houas, A.; Lachheb, H.; Ksibi, M.; Elaloui, E.; Guillard, C.; Herrmann, J. M. *Appl. Catal., B* **2001**, *31*, 145.

(23) Asahi, R.; Morikawa, T.; Ohwaki, T.; Aoki, K.; Taga, Y. *Science* **2001**, *293*, 269.

(24) Belhekar, A. A.; Awate, S. V.; Anand, R. *Catal. Commun.* **2002**, *3* (10), 453.

(25) (a) Tao, X.; Ma, W.; Zhang, T.; Zhao, J. *Angew. Chem.* **2001**, *113*, 3103. (b) Falconer, J. L.; Magrini-Bair, K. A. *J. Catal.* **1998**, *179*, 171.

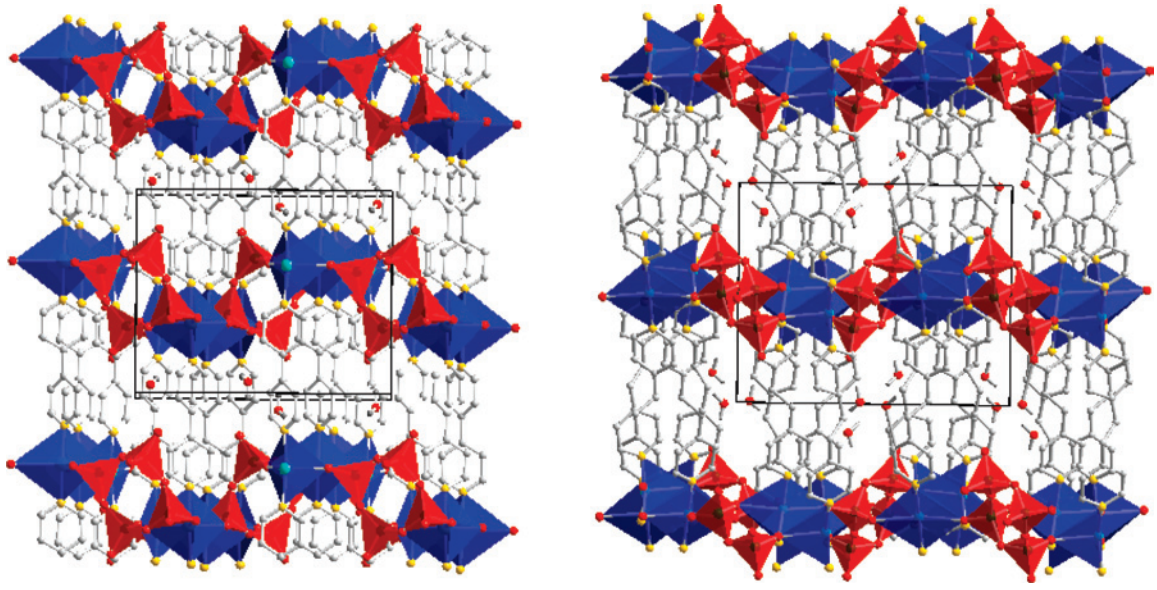

Figure 1. Structures of $[Ag(bpy)]_4V_4O_{12}\cdot 2H_2O$ (**I**) (left) and $[Ag(dpa)]_4V_4O_{12}\cdot 4H_2O$ (**II**) (right) viewed down the ~[001] direction of the unit cells (outlined). Blue polyhedra = Ag-centered coordination environments, red polyhedra = VO_4, red spheres = O, yellow spheres = N, white spheres = C, and light-blue spheres = Ag.

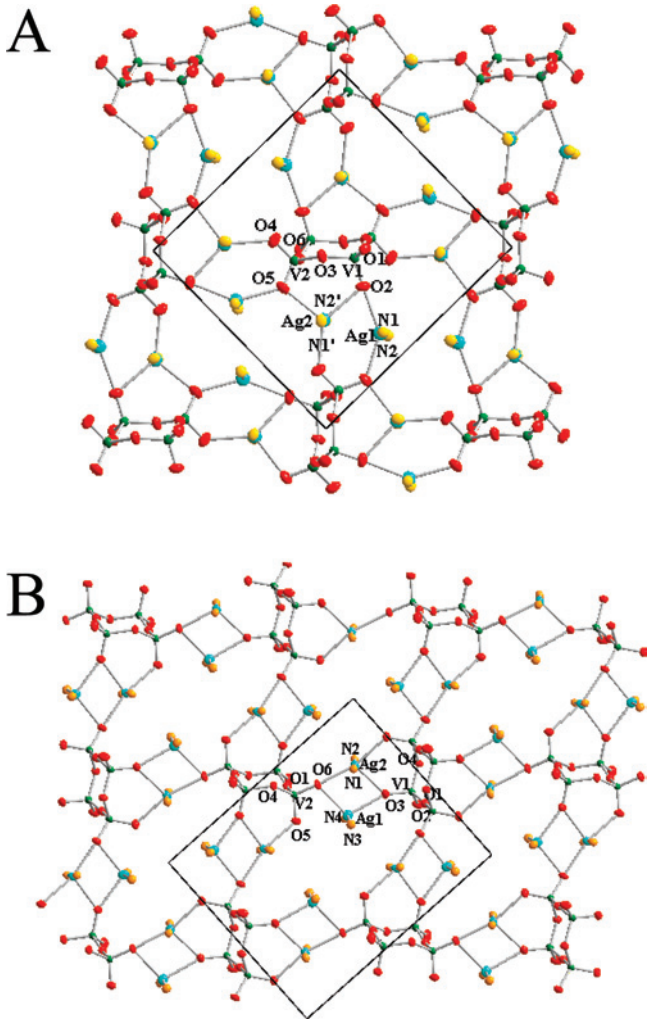

Figure 2. Structural view of a single "$AgVO_3$" layer in **I** (A) and **II** (B), drawn using 80% probability thermal ellipsoids and with symmetry-unique atoms labeled.

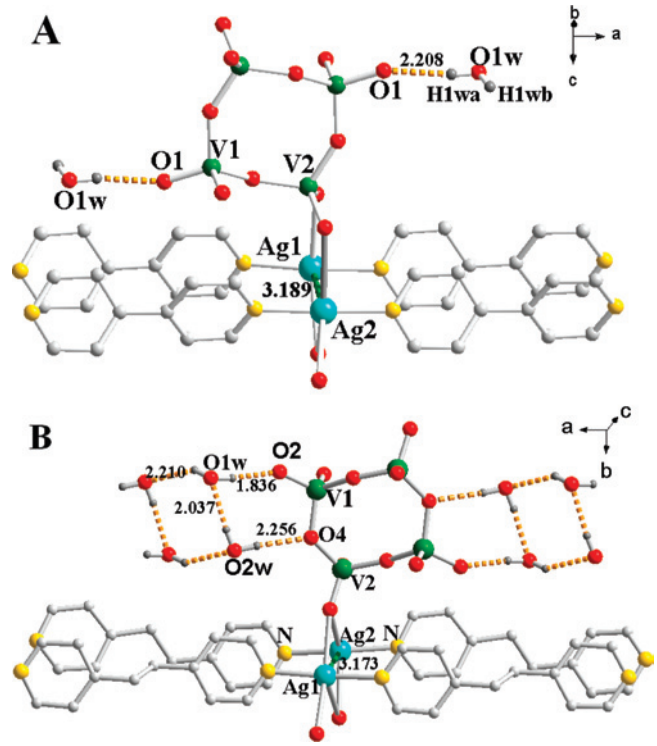

Figure 3. Structural view of the $\{V_4O_{12}\}^{4-}$ rings and $\{Ag(L)^+\}_n$ chains of **I** (A) and **II** (B) with labels for hydrogen bonds and the shortest Ag1···Ag2 distances. All atom types are labeled.

(11.375(2) Å) and a smaller interlayer spacing that can accommodate only two water molecules per formula. In II, however, the longer dpa bridging ligand and *a*-axis length (13.5748(3) Å) yields larger interlayer galleries that can accommodate four water molecules per formula. As shown in Figure 3, each $\{V_4O_{12}\}^{4-}$ ring in **I** is hydrogen-bonded to two H_2O molecules both above and below at a distance of 2.208(3) Å (O1···H1w) and at an angle of 168.99(1)° (O1−H1w−O1w). In **II**, the four H_2O molecules are hydrogen bonded into tetrameric clusters at distances of

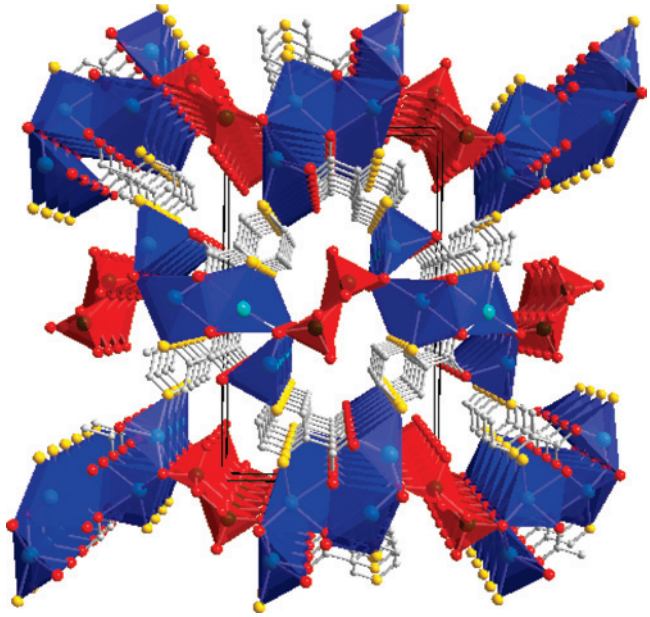

Figure 4. Polyhedral structural view of $Ag_4(pzc)_2V_2O_6$ (**III**) down the [100] direction of the unit cell (outlined). Blue polyhedra = Ag-centered coordination environments, red polyhedra = VO_5, red spheres = O, yellow spheres = N, white spheres = C, and light-blue spheres = Ag. All H atoms are omitted for clarity.

2.037(1) Å (O1w···H2w) and 2.210(1) Å (O2w···H1w). Each tetrameric water cluster is further hydrogen-bonded to two terminal O2 groups and to two bridging O4 groups of the $\{V_4O_{12}\}^{4-}$ rings (both above and below) at distances of 1.836(1) Å (O2···H1w) and 2.256(1) Å (O4···H2w). Thus, the structure of **II** provides larger intergallery spaces owing to the longer dpa bridging ligands, and which represents a valuable strategy for increasing the absorption capacity of small molecules within the micropores of hybrid solids.[2]

The structure of $Ag_4(pzc)_2V_2O_6$ (**III**) (pzc = pyrazinecarboxylate) is dissimilar to that of **I** and **II**, and is composed of a three-dimensional $\{Ag_2(pzc)^+\}_n$ coordination network that contains $\{VO_3^-\}_n$ double chains within its open channels, as shown in Figure 4. The structure may also be roughly viewed as containing heterometallic $\{Ag_2VO_3\}_n^{n+}$ layers that are bridged to each other through the coordination of pzc ligands to the Ag sites in each layer. The structure is more condensed than in **I** or **II** owing to the shorter pzc ligands, and thus, there are no internal lattice water molecules. The local coordination geometries of all symmetry-unique silver and vanadium atoms in **III** are plotted in Figure 5. The metavanadate $\{VO_3^-\}_n$ chains are remarkably similar to that found in $Ni(VO_3)_2 \cdot 4H_2O$[26] and consist of square-pyramidal (VO_5) polyhedra condensed via edge-sharing into zigzag chains that are aligned along the *a*-axis direction. In **III**, these $\{VO_3^-\}_n$ chains run parallel to the silver-oxide chains, shown in Figure 6. The VO_5 polyhedra are highly distorted, with V−O distances (1.63(1)−2.03(1) Å; Table 2) consistent with those in previously reported metavanadate chains. The calculated bond valence sums ($\sum S_{ij}$)[21] for vanadium, also

(26) Baudrin, E.; Touboul, M.; Nowogrocki, G. *J. Solid State Chem.* **2000**, *152* (2), 511–516.

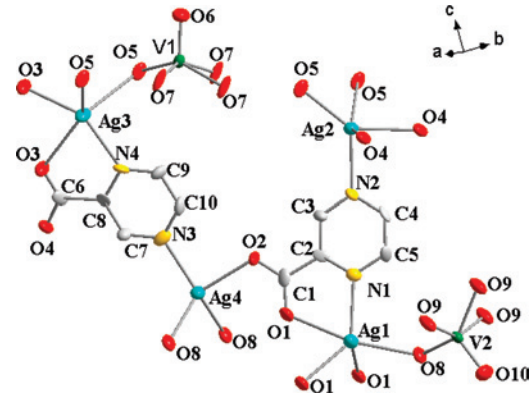

Figure 5. Structural view of the local coordination environments of all atoms in **III**, with all atoms labeled and thermal ellipsoids drawn at an 80% probability level.

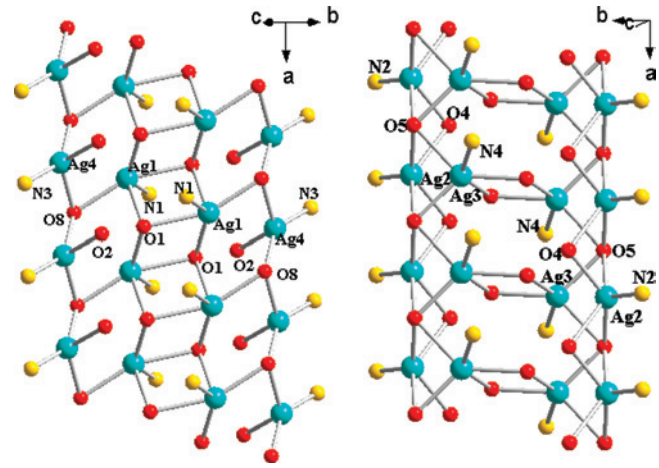

Figure 6. Structural views of the two different silver-oxide chains in **III**, containing Ag1/Ag4 (left) and Ag2/Ag3 (right), with selected atoms labeled.

listed in Table 2, are consistent with a fully oxidized +5 oxidation state.

The silver-organic network consists of four crystallographically-independent Ag atoms, comprising Ag1, Ag2, and Ag3 with distorted square-pyramidal $\{AgNO_4\}$ coordination geometries and Ag4 with a distorted tetrahedral $\{AgNO_3\}$ coordination geometry. As shown in Figure 6, the coordination polyhedron of each Ag site is linked to others via corner- and edge-sharing to form infinite metavanadate chains along the *a*-axis direction. Specifically, the square pyramidal Ag1 polyhedra share edges with each other via the O1 groups from the pzc ligands and form infinite double chains. Next, these infinite Ag1 double chains are condensed via corner-shared O8 groups to the tetrahedral Ag4 chains that are also connected via the O8 vertices. The other infinite chain containing Ag2 and Ag3 is, by contrast, formed from square-pyramidal double chains of Ag2 polyhedra. These chains are connected to edge-sharing square-pyramidal Ag3 dimers via two O5 groups, and are in turn shared with a neighboring vanadate chain. These two silver-oxide chains (Ag1/Ag4 and Ag2/Ag3) are bridged to each other through the multidentate pzc ligands to form the full three-dimensional network.

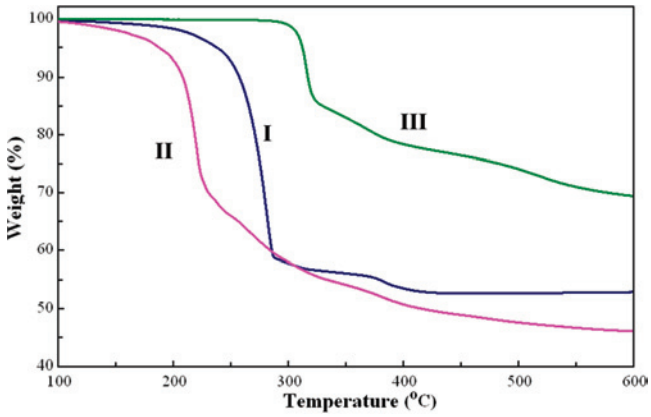

Figure 7. Thermogravimetric analyses of **I**, **II**, and **III**, plotted as weight (%) versus temperature (°C).

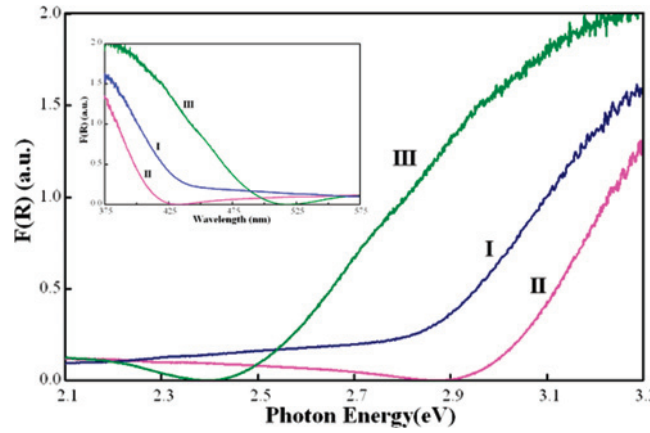

Figure 8. UV−vis diffuse reflectance spectra of **I**, **II**, and **III** plotted as a function of the photon energy in eV and as a function of wavelength in nm (inset).

Thermogravimetric Analyses and Reversible Water Absorption. The thermal stabilities, decomposition pathways, and reversible water absorption (i.e., microporosity) were probed in this series of three new vanadate hybrid solids. As an initial check of their full decomposition pathway, each sample was slowly heated to 600 °C under flowing N_2, and the changes in the structure and final products were characterized using Powder X-ray Diffraction (PXRD). The Thermogravimetric Analysis (TGA) of **I** exhibited a major weight loss of ∼42% from ∼180−300 °C, corresponding to the loss of both the lattice water and the bipyridine ligands (calcd 43%), shown in Figure 7. A second minor weight-loss step of 7% was observed from 300−430 °C and likely corresponds to the reduction of Ag^+ to Ag(s) and the loss of O_2 (calcd 8% for one O_2 per formula). The final black residue of **I** was determined by PXRD to be a mixture of Ag and VO_x (see Supporting Information). The TGA result for **II** is similar to that of **I**, with a major weight loss corresponding to the removal of four lattice water molecules and dpa ligands by ∼300−350 °C (exp. 48%; calcd 49%), followed by the loss of about one O_2 per formula (exp. 6%; calcd 7%). As before, the final black residue was found by PXRD to be a mixture of Ag and VO_x. For **III**, the loss of the pzc ligand occurs within a broad temperature range between 300−500 °C (exp. 27%; calcd 28%). The compound also exhibits a higher thermal stability than either **I** or **II**. Typically, the presence of more strongly-bonded carboxylate ligands in the structure results in a greater thermal stability, such as reported in the comparison of the thermal stability of $CuReO_4(pyz)$ versus $Cu_3ReO_4(q6c)$.[8]

For both $[Ag(bpy)]_4V_4O_{12}\cdot 2H_2O$ (**I**) and $[Ag(dpa)]_4V_4O_{12}\cdot 4H_2O$ (**II**), it is expected that the lattice water molecules located in the gallery spaces could be relatively easily removed without the concurrent loss of organic ligands or loss of sample crystallinity. After 6 h at 180 °C the crystalline powder of **I** can be completely dehydrated with the retention of a very similar crystalline structure, as evidenced by the PXRD results that show a small shifting of the diffraction peak positions (see Supporting Information). This dehydrated powder can be completely rehydrated in an aqueous solution at 140 °C. An almost identical PXRD pattern as before the dehydration is obtained, demonstrating the integrity of the structure during both the dehydration and rehydration steps. By contrast, the complete dehydration of **II** can be achieved at only 100 °C after 6 h, but which induces an irreversible change in the structure and cannot be rehydrated under similar conditions as found for **I**.

Optical Bandgap Sizes and Electronic Structures. As we have reported previously,[8] heterometallic oxides containing transition metals with both d^0 and d^{10} electron configurations, such as $MM'O_3$ (M = Cu, Ag; M′ = V, Nb, Ta),[13,14] exhibit small optical bandgap sizes with the absorption of visible-light energies that can be used to drive photocatalytic reactions. The hybrid solids **I**, **II**, and **III** are related to these condensed heterometallic oxides but contain either two- or three-dimensional "Ag_xVO_3" layers. These layers can function as the light-absorbing structural components as well as serve as the potential sites for photocatalytic reactivity. The UV−vis diffuse reflectance of each was measured and is shown in Figure 8. The absorption edge of each sample fell within or near the visible range of wavelengths, with approximate optical bandgap sizes of 2.77 eV for **I**, 2.95 eV for **II**, and 2.45 eV for **III**. By comparison, in the case of "organic free" α-$AgVO_3$ the optical bandgap edge occurs at ∼2.5 eV owing to an electronic excitation from the Ag-4d/O-2p to the empty V-3d orbitals.[13]

Calculations of the electronic structures of $[Ag(bpy)]_4V_4O_{12}\cdot 2H_2O$ (**I**), $[Ag(dpa)]_4V_4O_{12}\cdot 4H_2O$ (**II**), and $Ag_4(pzc)_2V_2O_6$ (**III**) were performed to evaluate the atomic-orbital contributions to the valence and conduction bands and to understand the structural factors that influence the sizes of their optical band gaps. Shown in Figure 9 is the calculated total Densities-Of-States (DOS), and overlaid is the partial DOS contributions from each constituent element of the solid. In all three hybrid solids the lowest unoccupied crystal orbitals of the conduction band were confirmed to derive from the V 3d orbitals, consistent with prior results reported for the condensed α-$AgVO_3$. Also, the highest occupied crystal orbitals of all three are closely similar and are formed primarily from contributions from the Ag 4d, N 2p, and O 2p orbitals. The same general trend in bandgap sizes is reproduced as found in the UV−vis DRS measurements,

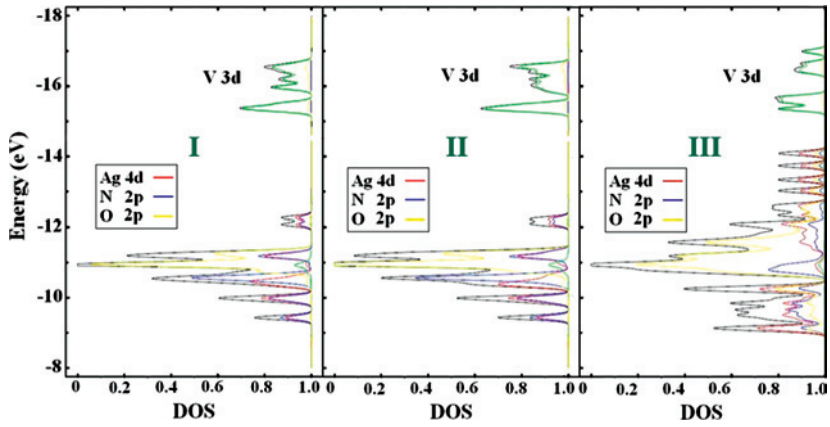

Figure 9. Calculated total and projected densities-of-states (DOS) for all three solids.

which decreases from **II** to **I** to **III**. This ordering of their bandgap sizes can be understood as a result of changes in both the local coordination geometries and the degree of the structural connectivity. The vanadate structures in **I** and **II** contain isolated tetrameric rings consisting of VO_4 tetrahedra, which lead to a relatively small amount of conduction band broadening and a larger bandgap size. The structures of α-$AgVO_3$ and **III**, by contrast, contain infinite edge-sharing chains of VO_5 polyhedra. This leads to relatively greater conduction band widening and the decreased bandgap size. In an analogous fashion, the valence bands are relatively wider in **II** and **I** compared to those in α-$AgVO_3$ and **III**. This is caused by going from the dimers of $Ag(L)^+$ chains in **I** and **II** to the much larger clusters of extended chains in α-$AgVO_3$ and **III**. Thus, these results help to understand the effect of the "Ag_xVO_3" structural connectivity upon the bandgap sizes, and which is governed by the choice of the size and coordination preference of the organic ligand.

Photocatalytic Decomposition Reactions. MB is commonly used as a representative of widespread organic dyes that contaminate textile effluents and that are very difficult to decompose in waste streams under visible-light irradiation.[22−25] Herein, MB was used as a model organic dye to evaluate the photocatalytic activities of the three new hybrid solids toward the decomposition of organic pollutants. Owing to their different bandgap sizes, the photocatalytic reaction of $[Ag(bpy)]_4V_4O_{12}\cdot 2H_2O$ (**I**) and $[Ag(dpa)]_4V_4O_{12}\cdot 4H_2O$ (**II**) should take place under only ultraviolet light (λ < 400 nm), while $Ag_4(pzc)_2V_2O_6$ (**III**) should be active under both ultraviolet and visible-light (λ > 400 nm) irradiation. During the course of the photocatalytic reactions the stability of the hybrid solids was monitored using PXRD (see Supporting Information). The PXRD confirmed that the crystal structures of the hybrid solids were unaltered, and the powders remained stable under these testing conditions.

The photocatalytic reactions were performed as described in the Experimental Section. As shown in Figure 10, changes in the concentration of the aqueous MB solution were plotted versus irradiation time. As a control, simple photolysis experiments of the MB solution were also performed under the same conditions without the use of the hybrid solids. The results show that **I**, **II**, and **III** are all active for the decomposition of MB under UV light irradiation, with rates

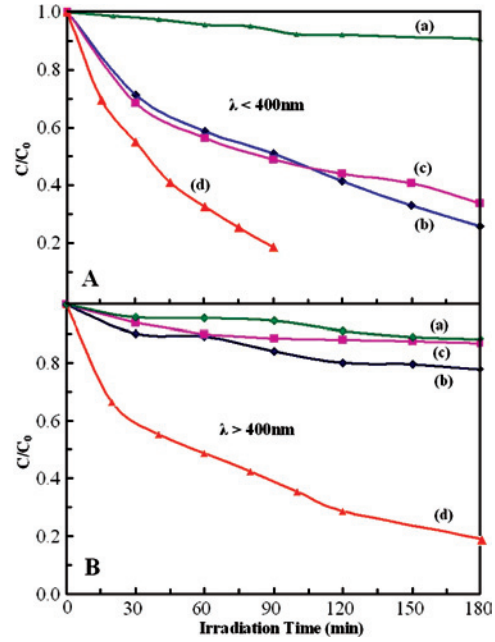

Figure 10. Photocatalytic decomposition of MB solutions (6.0 mg/L, 50 mL) using 150 mg of the three silver vanadates, either under UV (A; upper) or under visible-light (B; lower) irradiation for **I** (b), **II** (c), **III** (d). Photolysis of the ligand by itself is labeled (a).

of 1.01, 0.64, and 2.65 mg L^{-1} h^{-1} respectively. During the first 30 min there is a faster rate of removal of MB from solution owing to its adsorption to the particle surfaces. This initial rate increases as expected with increasing amounts of solid sample used in the photocatalytic reaction. Thus, the first 30 min of the photocatalytic reaction was not included in the rate calculation. After 3 h of irradiation, approximately 70% and 65% of MB has been decomposed with the use of 150 mg of **I** and **II**, respectively. Neither sample is active under visible-light irradiation. By contrast, the lower-energy bandgap of **III** enables the decomposition of 80% of the MB after only 3 h under only visible-light irradiation, Figure 10B, with a rate of 1.20 mg L^{-1} h^{-1}. Shown in Figure 11 is the evolution of the MB absorption spectra versus time in the presence of 150 mg of **III** under visible light irradiation, which illustrates the decreasing concentration of MB over time. Notably, the photocatalytic rate of **III** under either ultraviolet or visible light is higher than either **I** or **II**. These results suggest that the more extended network of **III**, that

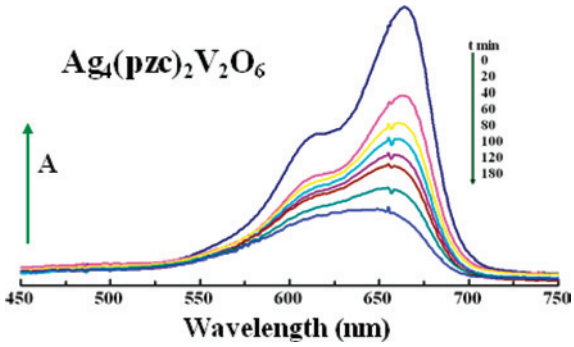

Figure 11. Absorption spectra of a solution of MB (6.0 mg/L, 50 mL) during a photocatalytic test reaction using 150 mg of **III** under visible light irradiation.

is, the vanadate chains as well as the much larger clusters of Ag-oxide/organic chains, aids in the transport of excited holes/electrons to the surface to initiate the photocatalytic decomposition reaction with MB. More generally, these results also show that more reactive hybrid photocatalysts can be achieved as a result of a better ability to tune the structural features and optical properties of heterometallic oxides with the use of suitable organic ligands.

Conclusions

A series of three new silver-vanadate hybrid solids, $[Ag(bpy)]_4V_4O_{12}\cdot 2H_2O$ (**I**), $[Ag(dpa)]_4V_4O_{12}\cdot 4H_2O$ (**II**), and $Ag_4(pzc)_2V_2O_6$ (**III**), has been synthesized via hydrothermal methods. All three hybrid solids are composed of silver-vanadate layers pillared by the organic ligands (bpy, dpa, and pzc) via coordination to the silver sites. The structures of **I** and **II** contain $Ag(L)^+$ (L = bpy, dpa) chains and tetrameric $\{V_4O_{12}\}^{4-}$ rings, while **III** is found to be constructed from two different extended $\{Ag_4N_4O_6\}$ chains and also zigzag $\{VO_3^-\}_n$ chains. The TGA analysis of each shows the removal of water, followed by ligands, at >180 °C for **I**, >120 °C for **II**, and at >300 °C for **III**. Further, hybrid **I** exhibits microporosity with the reversible absorption of lattice water molecules at the low temperatures of ~140−180 °C. Their measured optical bandgap sizes decrease from **II** (2.95 eV) to **I** (2.77 eV) to α-$AgVO_3$ (2.5 eV) to **III** (2.45 eV), owing to the changes in the extended network dimensionality. Photocatalytic studies have been used to demonstrate that the new silver-vanadate hybrids can efficiently decompose MB. The photocatalytic activities of **I** and **II** are limited to UV light owing to their large bandgap sizes, while **III** is active under visible-light irradiation because of its smaller bandgap size. These results demonstrate the significant utility of using organic ligands for control over the atomic- and electronic-structures of heterometallic oxides to both understand and modify their photocatalytic properties.

Acknowledgment. Acknowledgment is made to the donors of the American Chemical Society Petroleum Research Fund (#46803-AC10), the Beckman Young Investigator Program (P.A.M.) of the Beckman Foundation, and the Chemical Sciences, Geosciences and Biosciences Division, Office of Basic Energy Sciences, Office of Science, U.S. Department of Energy (DE-FG02-07ER15914) for support of this research, and also for assistance with the collection of single crystal X-ray data (P. Boyle).

Supporting Information Available: Crystallographic data for **I**, **II**, and **III** in CIF format, and powder X-ray diffraction results for all prepared compounds including for the as-synthesized hybrids, for their TGA residues, for the dehydrated/rehydrated analogues of **I**, and for all three samples during the photocatalytic reactions. This material is available free of charge via the Internet at http://pubs.acs.org.

IC8004129